Title

Versatile and Highly Efficient Controls of Reversible Topotactic Metal–Insulator Transitions through Proton Intercalation

Journal

Advanced Functional Materials, 29(50)

ISSN

1616-301X

Authors

Chen, Shanquan
Zhou, Haiping
Ye, Xing
et al.

Publication Date

2019-12-01

DOI

10.1002/adfm.201907072

Peer reviewed

Versatile and Highly Efficient Controls of Reversible Topotactic Metal–Insulator Transitions through Proton Intercalation

Shanquan Chen, Haiping Zhou, Xing Ye, Zuhuang Chen, Jinzhu Zhao, Sujit Das, Christoph Klewe, Lei Zhang, Eduardo Lupi, Padraic Shafer, Elke Arenholz, Dun Jin, Haoliang Huang, Yalin Lu, Xiaowen Li, Meng Wu, Shanming Ke, Hu Xu, Xierong Zeng, Chuanwei Huang, Lane W. Martin, and Lang Chen*

The ability to tailor a new crystalline structure and associated functionalities with a variety of stimuli is one of the key issues in material design. Developing synthetic routes to functional materials with partially absorbed nonmetallic elements (i.e., hydrogen and nitrogen) can open up more possibilities for preparing novel families of electronically active oxide compounds. Fast and reversible uptake and release of hydrogen in epitaxial ABO_3 manganite films through an adapted low-frequency inductively coupled plasma technology is introduced. Compared with traditional dopants of metallic cations, the plasma-assisted hydrogen implantations not only produce reversibly structural transformations from pristine perovskite (PV) phase to a newly found protonation-driven brownmillerite one but also regulate remarkably different electronic properties driving the material from a ferromagnetic metal to a weakly ferromagnetic insulator for a range of manganite ($La_{1-x}Sr_xMnO_3$) thin films. Moreover, a reversible perovskite-brownmillerite-perovskite transition is achieved at a relatively low temperature ($T \leq 350$ °C), enabling multifunctional modulations for integrated electronic systems. The fast, low-temperature control of structural and electronic properties by the facile hydrogenation/dehydrogenation treatment substantially widens the space for exploring new possibilities of novel properties in proton-based multifunctional materials.

1. Introduction

Functional solid-state materials with novel structures lay the foundation for the sustainable development of modern electronic technologies. The ability to tailor a new crystalline structure and associated functionalities with a variety of stimuli is one of the key issues in material design. Developing synthetic routes to functional materials with partially absorbed nonmetallic elements (i.e., hydrogen and nitrogen) could open up possibilities for preparing novel families of electronically active oxide compounds. Hydrogen, the smallest and lightest element, has been readily incorporated in materials to induce diverse phase transformations and give rise to unprecedented electronic properties.[1,2] Highly contrasting electronic properties have emerged,[3–10] reflecting the decisive role of hydrogen implantation in determining the crystalline structure and physical properties of a wide variety of functional materials. In particular, such delicate

S. Q. Chen, D. Jin, Dr. S. Ke, Prof. X. Zeng, Dr. C. W. Huang
Shenzhen Key Laboratory of Special Functional Materials
College of Materials Science and Engineering
Shenzhen University
Shenzhen 518060, China
E-mail: cwhuang@szu.edu.cn

S. Q. Chen, Prof. Z. H. Chen
School of Materials Science and Engineering
Harbin Institute of Technology
Shenzhen 518055, China

Prof. H. P. Zhou, X. Ye
School of Materials and Energy
University of Electronic Science and Technology of China
Chengdu 611731, China

Dr. J. Zhao, X. Li, Prof. H. Xu, Prof. L. Chen
Department of Physics
Southern University of Science and Technology
Shenzhen 518055, China

Dr. S. Das, Dr. C. Klewe, Dr. L. Zhang, E. Lupi, Prof. L. W. Martin
Department of Materials Science and Engineering
University of California
Berkeley, CA 94720, USA

Dr. C. Klewe, Dr. P. Shafer, Dr. E. Arenholz
Advanced Light Source
Lawrence Berkeley National Laboratory
Berkeley, CA 94720, USA

Dr. H. Huang, Prof. Y. Lu
National Synchrotron Radiation Laboratory
University of Science and Technology of China
Hefei 230026, China

Dr. M. Wu
Department of Physics
Xiamen University
Xiamen 361005, China

engineering has been embodied incisively and vividly in transition-metal oxides accompanied by emergent multitudinous behaviors, including strong modulations of magnetic ordering, metal-to-insulator transitions, and superconductivity.[3,6–8]

Functional oxides, particularly, the perovskite oxides (ABO_3), with flexibly adjustable crystalline structures and a wide ranges of functionalities, including ferroelectricity, ferromagnetism, multiferroicity, superconductivity, metal-to-insulator transitions, etc. have attracted extensive attention in past decades.[11–16] The remarkable modulations of the electronic functionalities of perovskites (PVs) have been largely achieved via misfit strain,[17–23] metallic-cation doping,[11,24] oxygen atmosphere,[25–29] crystallographic orientation,[30–33] and film thickness.[19,34–36] Previous studies have mainly focused on chemical doping either into the *A* or *B* site with inorganic metallic cations.[11,24,37,38] Very recently, the search for new functionalities through nonmetallic elemental doping (e.g., hydrogen and nitrogen) as cation or anion in perovskite oxides has become highly active[5,8,9,39,40] as a result of the different ionic radii, charge, and electronegativity among oxygen, nitrogen, and hydrogen.[8,41–44] This rational synthesis strategy has recently provided an alternative approach to effectively tune structural and chemical varieties and the consequential functionalities of complex-oxide compounds.[6,8,39,41,45–47] These methods, however, generally involve time-consuming processes (i.e., several hours) or high-temperature annealing ($T > 400$ °C) in to achieve the desired effects.[3,5,41,48] The sluggish chemical conversion and high-temperature environment required for hydrogen or nitrogen implantation are unrealistic for technological applications.

Herein, an adapted low-frequency inductively coupled plasma (LFICP) technology, generating active hydrogen plasmas with high density and radical ionization,[49] is employed to realize a fairly low-temperature ($T \leq 300$ °C) and fast hydrogen implantation process (i.e., within a few minutes) in various manganite $La_{1-x}Sr_xMnO_3$ (LSMO, $x = 0.2$, 0.3, and 0.7) thin films. Compared with traditional dopants of metallic cations, the plasma-assisted hydrogen implantations not only produce reversibly structural transformations from pristine PV ($La_{1-x}Sr_xMnO_{3.0}$) to protonation-driven brownmillerite (HBM, $H_yLa_{1-x}Sr_xMnO_{2.5}$, HLSMO) structures (**Figure 1**) but also regulate remarkably different electronic properties driving the material from a ferromagnetic metal to a weakly ferromagnetic insulator. It is revealed via first-principles calculations that the stable crystalline structure of hydrogenated HBM phase of HLSMO films contains alternate octahedral layer, and pyramidal and plane layers, in sharp contrast to the previously reported octahedral/tetrahedral geometry for materials with brownmillerite (BM) phase. This fast and facile modulation of crystalline structure and physical properties via hydrogenation substantially widens the space for exploring more novel structures and functionalities in functional oxides.

2. Results and Discussion

Here, we first deposited PV LSMO [$x = 0.3$, LSMO(7/3)] films on (001)-oriented $SrTiO_3$ (STO), $LaGaO_3$ (LGO), and $(LaAlO_3)_{0.3}$-$(Sr_2AlTaO_6)_{0.7}$ (LSAT) single substrates by pulsed-laser deposition (PLD) (details in the Experimental Section). In order to determine the structural changes, we performed X-ray diffraction (XRD) measurements on both pristine and the hydrogen-plasma-treated manganite films. **Figure 2**a shows the XRD θ–2θ scans of the pristine LSMO(7/3) heterostructures deposited in an oxygen pressure of 15 Pa (i.e., LSMO(7/3)/LSAT, LSMO(7/3)/LGO, and LSMO(7/3)/STO), which exhibit high-quality perovskite without impurity phases. The corresponding out-of-plane lattice parameter *c* of LSMO(7/3) thin films (black curve, Figure 2c) is gradually decreased (3.893, 3.860, and 3.855 Å, respectively) due to the tunable misfit stains from the various substrates, relative to bulk LSMO(7/3) ($c = 3.876$ Å). The as-grown perovskite LSMO(7/3) films were then treated by hydrogen-plasma injection in a LFICP system. After a low-temperature and fast hydrogenation process (i.e., 300 °C and 10 min), the diffraction peaks of the films (Figure 2a) considerably shifted toward a lower angle position, accompanied by an additional peak at ≈32° emerging. Meanwhile, a doubling of the *c* lattice is obviously displayed in the treated HLSMO films, stemming from the alternative stacking of octahedral and tetrahedral sub-layers along the film-deposition direction. This diffraction pattern signifies a typical BM phase.[28] Note

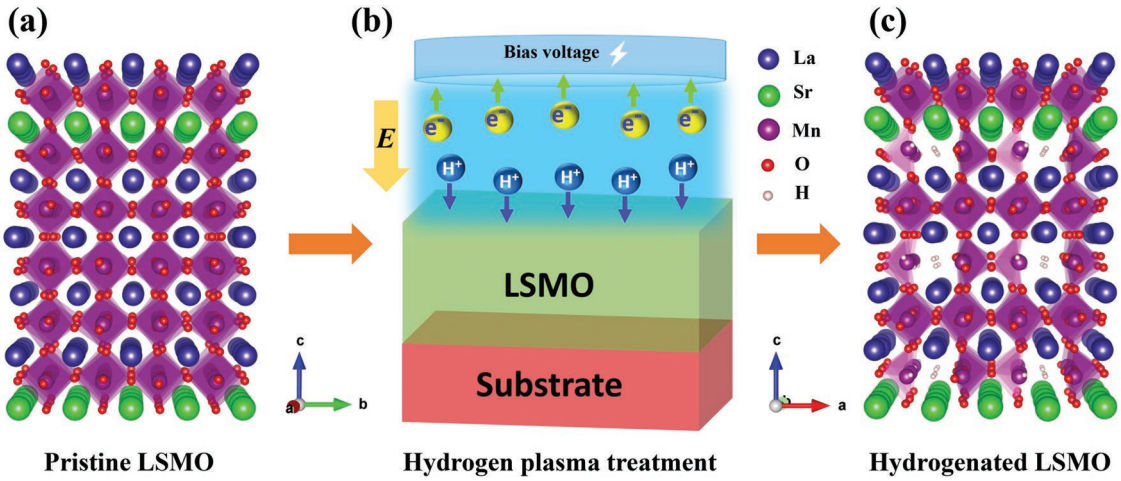

Figure 1. Schematics of LSMO films a) before (pristine perovskite) and c) after hydrogenation (brownmillerite) via b) hydrogen plasma treatments.

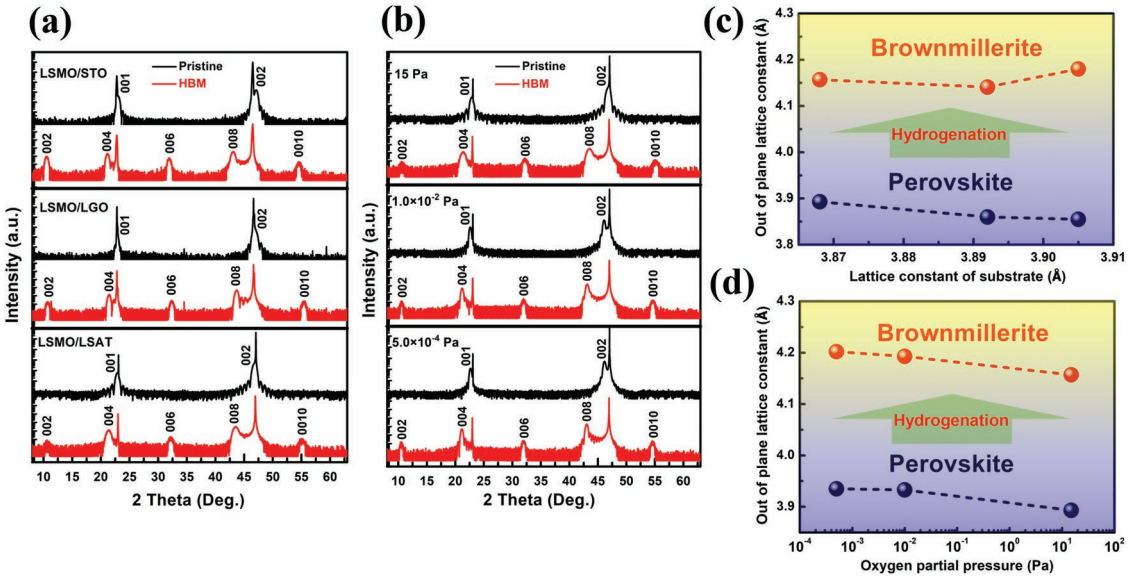

Figure 2. XRD θ–2θ patterns and evolution of the c lattice for pristine and hydrogenated a,c) LSMO (7/3) films grown on STO (a = 3.905 Å), LGO (a = 3.892 Å), and LSAT (a = 3.868 Å) substrates and b,d) LSMO(7/3)/LSAT systems deposited with different oxygen pressures (5.0×10^{-4}, 1.0×10^{-2}, and 15.0 Pa).

that the c lattice (with pseudocubic lattice parameter of 4.18 Å) further increases in the newly found HBM phase of hydrogenated HLSMO(7/3) films, compared to the conventional oxygen-vacancy-induced BM phase (c = 4.11 Å).[48] This fast ($t \leq 10$ min) PV-HBM conversion due to the high-chemical reactivity of the hydrogen plasma has not been widely explored, in sharp contrast to the previously extensively reported time-consuming (up to several days and above 500 °C) thermal process.[48,50] We also stress that the HBM phase is stable over long times (at least 50 d or more) in ambient atmospheres (Figure S2, Supporting Information). More importantly, we further examine the applicability of the present method, which can be generally applied to various LSMO manganite heterostructures. For example, the rapid PV-HBM transitions were realized in different manganite heterostructures [i.e., LSMO(7/3)/STO, LSMO(7/3)/LGO, and LSMO(7/3)/LSAT in Figure 2a,c] or the LSMO(7/3)/LSAT systems synthesized in various oxygen pressures (i.e., 5.0×10^{-4}, 1.0×10^{-2}, and 15.0 Pa shown in Figure 2b,d). These findings contrast with the previous results, which claimed that the occurrence of BM phase has a particular relationship with the oxygen content of the pristine LSMO films.[50] More interesting, the present versatile plasma process also enables similar topotactic transformations in other $La_{1-x}Sr_xMnO_3$ (for example, x = 0.2 and 0.7) epitaxial systems, demonstrating a clear HBM phase in $La_{0.8}Sr_{0.2}MnO_3/LaAlO_3$ and $La_{0.3}Sr_{0.7}MnO_3/LaAlO_3$ systems (Figure S1, Supporting Information). We note that there is no apparent peak position change in any of the substrates involved, suggesting a negligible effect of the hydrogenation process on the substrates. Thus, this low-temperature hydrogenation process, as a fast and efficient way to achieve a topotactic transformation, can be applied to various epitaxial manganite heterostructures while being insensitive to the chemical compositions, substrates, and oxygen-deposition pressure.

To obtain more information on the structural modulation, the dynamic evolution between PV and HBM phases was further characterized. It is found that the hydrogen plasma-induced HBM phases in the LSMO films can be readily restored back to the initial perovskite phase via simple oxygen annealing in a relatively low temperature (300 °C) environment. **Figure 3**a shows the reversible topotactic transitions in the LSMO(7/3)/STO system through the hydrogenation/dehydrogenation processes. Compared with the as-grown counterpart, the (00l) peak of the hydrogenated HLSMO(7/3) films shifts to a lower angles, indicating an increasing c lattice up to ≈4.18 Å. The c lattice reduces to 3.858 Å after annealing at 300 °C, suggesting a recovery to the perovskite structure (PV'). To further determine the strain states of the LSMO(7/3)/STO heterostructures, reciprocal space mapping (RSM) measurements (Figure 3b) were conducted. The results reveal that coherently strained, high-quality heterostructures with identical in-plane lattices are achieved (Figure 3c) in all of the pristine, hydrogenated, and annealed LSMO(7/3) films. Consequently, this lattice change during hydrogenation results in unit-cell volume expansion from 58.79 to 63.74 Å^3 (i.e., a change of ≈8.4%). From an application perspective, the hydrogenation/dehydrogenation induced reversible structural modulations presented here enable potential applications, such as hydrogen storage.[3] These findings derived here could deepen the current understanding and possibly offer insights to the reversible perovskite/brownmillerite phase transitions in oxide films of different structural states via facile hydrogenation/dehydrogenation processes.

Consequently, the hydrogenation process also has a great influence on the electrical and magnetic properties of the LSMO(7/3) films. As plotted in **Figure 4**a, significant changes were observed on the temperature-dependent in-plane magnetization (M–T curves) for pristine, hydrogenated (HBM phase), and dehydrogenated (annealed) LSMO(7/3) films. The Curie temperature (T_c) of the pristine LSMO(7/3) films is ≈340 K, consistent with previously reported values.[34,51] The ferromagnetism of the hydrogenated HLSMO(7/3) films with the HBM phase,

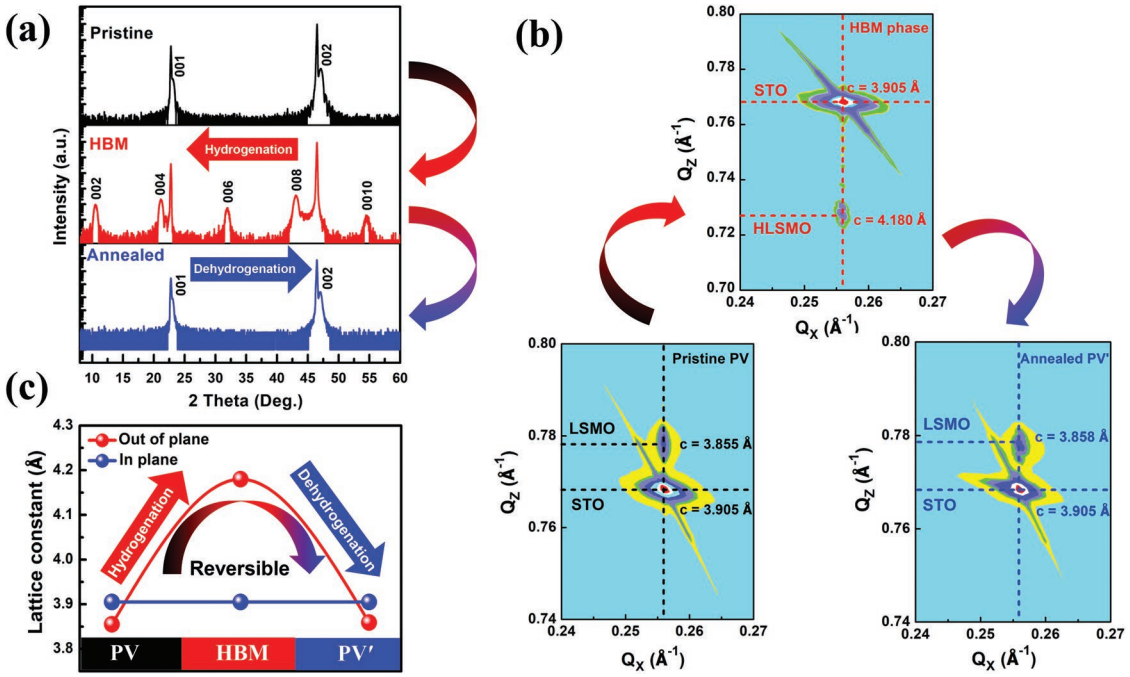

Figure 3. Structural evolution of LSMO(7/3) films via hydrogenation and dehydrogenation processes. a) XRD θ-2θ scans and b) RSM measurements around the (103) reflection for pristine, hydrogenated, and annealed LSMO(7/3) films. c) The epitaxy and lattice parameters for the reversible PV-HBM-PV' transformations of LSMO(7/3) films.

however, is dramatically suppressed, with a visible ferromagnetic signal retained up to only ≈100 K. A well-defined magnetic hysteresis loop arises as clearly shown in Figure 4b, providing evidence for the weak ferromagnetism in the newly found HBM phase in hydrogenated HLSMO(7/3) films. In contrast, no coercive field is detected in the conventional LSMO(7/3) films with the BM phase, as expected for this antiferromagnetic phase.[48] Notably, ferromagnetism with high $T_c \approx 340$ K can be fully restored after the low-temperature dehydrogenated process (i.e., oxygen annealing process) for the HLSMO(7/3) films. Compared with the antiferromagnetic BM phase, the saturated magnetization (M_s) (inset of Figure 4a) is 470, 35, and 480 emu cc^{-1} for pristine (PV), hydrogenated (HBM), and dehydrogenated (annealed, PV') phases, respectively. Clearly different magnetic properties are also observed (as shown at inset of Figure 4a) for the postannealing induced BM phase and the present hydrogenated HBM one, possibly attributed to the successful implantation of H^+ in the HLSMO films, as later

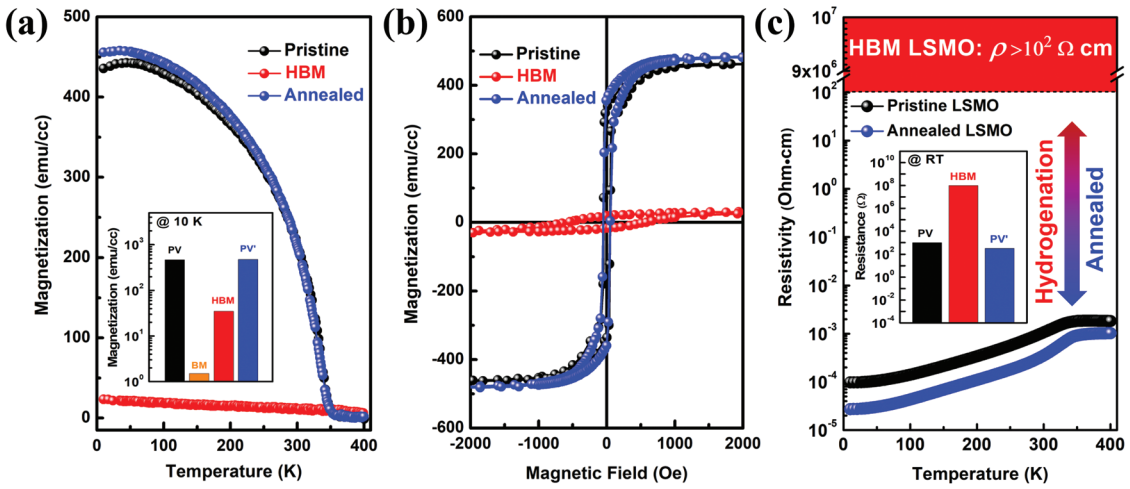

Figure 4. Temperature-dependent magnetic and electronic properties. a) Magnetization-temperature (M–T) curves (measured in the applied magnetic field of 500 Oe, parallel to the film plane). The inset shows the different saturated magnetizations among PV, BM (ref. [48]), HBM, and PV' (annealed) films measured at 10 K. b) Magnetic hysteresis (M–H) loops measured at 10 K with the magnetic field parallel to the film plane and c) temperature-dependent resistivity measured for pristine, hydrogenated (upper red region), and restored LSMO (7/3) films, the inset shows the tunable resistances of PV, HBM, and PV' (annealed) films measured at room temperature (RT).

confirmed by oxygen *K*-edge X-ray absorption s pectroscopy (XAS) measurement. Furthermore, the hydrogenation process simultaneously results in significant changes to the electrical transport of the LSMO(7/3) films. Compared with the metallic phase observed for pristine/annealed LSMO(7/3) films, the electrical transport measurements plotted in Figure 4c and the inset show that the resistivity of the hydrogenated HLSMO(7/3) films increases at least five orders of magnitude (i.e., exceeding the measurement range of the physical properties measurement system (PPMS)), revealing a metal-to-insulator transition via the hydrogen plasma treatment. Remarkably, this hydrogenation-induced insulating HBM phase in the HLSMO(7/3) films can readily be turned back to the metallic one by simply annealing in an oxygen atmosphere (i.e., at 300 °C, 1 h); a change also accompanied by the recovery of the crystalline structure and magnetic properties. Moreover, similar modulations of magnetic and electrical properties could be achieved in other LSMO(7/3) heterostructures (Figure S3, Supporting Information) via the hydrogenation/dehydrogenation process. Well defined magnetic hysteresis loops with different saturated magnetizations are demonstrated in all hydrogenated heterostructures (Figure S3a,b, Supporting Information). Similar enhanced resistivity was previously observed in the PV-BM phase transition of LSMO(7/3) films v ia e lectron-beam i rradiation in a transmission electron microscope.[29,52] Thus, the observed multilevel changes in magnetic and electrical properties among the PV, BM, HBM, and annealed PV' phases offer further evidence of the distinctive structural and electronic modulations in manganite thin films using hydrogen plasma.

To further determine the origin of the reversible structural transition and relevant modulations of electronic properties during hydrogenation/dehydrogenation, the content of hydrogen and the valence state of manganese in the hydrogenated HLSMO have been investigated (**Figure 5**). Secondary-ion mass spectrometry (SIMS) measurements were carried out to explore the hydrogen content in the heterostructures and revealed the successful incorporation of hydrogen into the HLSMO(7/3) films as compared to the pristine LSMO(7/3) films. More importantly, the hydrogen accumulates at the region of LSMO films near the substrates (light-green in Figure 5a), which is consistent with above XRD data (Figures 2 and 3) that no peak position shifts for the substrates. It has been reported theoretically that the H^+ ions are bonded to the apical O^{2-} ions in tetrahedral layers of hydrogenated oxide films within the HBM phase.[8] On the contrary, no distinctive gradient distribution of hydrogen was detected in the as-grown LSMO(7/3) films, reconfirming that no protonation has occurred at the substrate region. In combination with the oxygen-insensitive hydrogenation, as plotted in Figure 2b, hydrogen intercalation could be regarded as a major origin for oxygen extraction and the subsequent topotactic PV-HBM and electronic transformations in LSMO(7/3) films. The subsequent oxidation states of the elements in LSMO(7/3) films during hydrogenation/dehydrogenation were determined using soft XAS. To clearly evaluate the manganese valence state of the hydrogenated HLSMO(7/3) film, the spectra of bulk $SrMnO_3$ (i.e., Mn^{4+} reference), $LaMnO_3$ (i.e., Mn^{3+} reference), and MnO (i.e., Mn^{2+} reference) are plotted below the spectra of PV/HBM/PV' films (Figure 5b).[53,54] Drastic changes in spectra features indicate that the valence state of the manganese is clearly different for the pristine, hydrogenated (HBM phase), and dehydrogenated (annealed) LSMO(7/3) films (Figure 5b). These XAS spectra show mixed-valence Mn^{3+} and Mn^{4+} in the pristine LSMO(7/3) films, consistent with stoichiometric LSMO(7/3) films.[22] The peak position of the manganese *L*-edge shifts toward lower energy compared with the reference MnO spectrum, which implies a dominant presence of Mn^{2+} for the hydrogenated HLSMO(7/3) films. Thus, the estimated hydrogen content in HBM phase is roughly 0.3 (i.e., $y = 0.3$, as in $H_{0.3}La_{0.7}Sr_{0.3}MnO_{2.5}$), assuming the +1 state of hydrogen ions. This finding also reveals that the hydrogen content forms H^+ in the present system, in sharp contrast to the CaH_2 induced hydrogen anions H^-.[39] Meanwhile, this reduced valence of manganese from +3.3 to +2.0 accounts for the further inflated *c* lattice (4.18 Å, Mn^{2+}) of epitaxial hydrogenated HLSMO(7/3) within the HBM phase, compared with that (4.11 Å, $Mn^{2.3+}$) in the original BM phase. More importantly, the absorption spectra

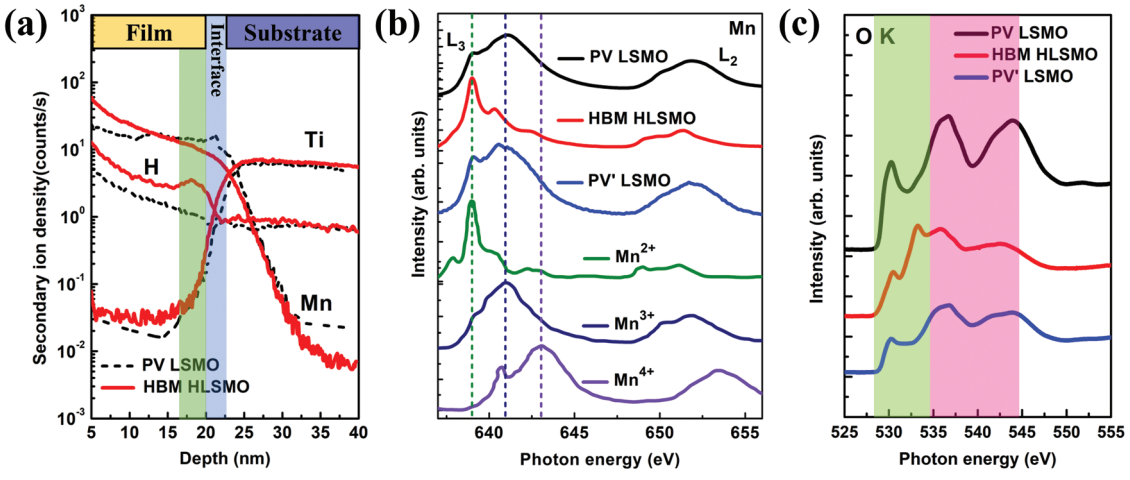

Figure 5. a) Depth profiles of H, Mn, and Ti ions for pristine LSMO and hydrogenated HLSMO films, measured with secondary-ion mass spectrometry (SIMS). XAS spectrum of b) the Mn L-edge and c) O K-edge of LSMO films (pristine, hydrogenated (HBM phase), and dehydrogenated (annealed, PV'). The light-green and pink shading in (c) represent the Mn—O and La/Sr—O hybridizations, respectively.

at the manganese *L*-edge of the annealed LSMO(7/3) films have been nearly recovered to that of the pristine LSMO(7/3). Variations of the oxygen *K*-edge spectra further support the presence of H^+, with significantly suppressed peak intensity in the HLSMO(7/3) films around 527–535 ev and significant peak shifts in the range of 535–545 ev, which are associated with weaker Mn—O bonds and La/Sr—O hybridizations, respectively. Altogether, these results support the observation of significant incorporation of H^+ which gives rise to the topotactic phase transformation and consequently variations of the manganese valence state, which results in deteriorated Mn—O orbital hybridizations and weakened ferromagnetism in the new-found HBM phase of hydrogenated LSMO(7/3) films. The BM phase of $ABO_{2.5}$ usually consists of alternate stacks of BO_4 (square plane, tetrahedra),[8,28] BO_5 (pyramid), or BO_6 (octahedra) layers.[55] Based on first-principles calculations, it is predicted that the optimized crystal structure of HBM phase of HLSMO films contains three types of Mn coordination geometries (i.e., an alternate stacking of octahedral layer, and pyramidal and plane layers along c axis, as shown in Figure S4, Supporting Information). This finding is in sharp contrast to the previously reported alternate octahedral/tetrahedral sub-layers for $ABO_{2.5}$ with BM phase.[28,29,48]

3. Conclusions

In summary, versatile modulations of the hydrogen uptake and release in epitaxial LSMO films could be achieved rapidly ($t \leq 10$ min) at low temperatures ($T \leq 300$ °C) by a highly efficient hydrogen-plasma treatment. The rapid and low-temperature protonation enables reversible structural phase transformations and distinctive electronic modulations, accompanied by a pronounced valence change of the manganese ions. A novel, weakly ferromagnetic insulating state was achieved in the hydrogenated HLSMO(7/3) films with a newly found HBM phase, consisting of alternate octahedral layer, and pyramidal and plane layers based on first-principles calculations. This facile hydrogenation/dehydrogenation process could open up new possibilities for multilevel phase modulations with rich functionalities and provide opportunities to design novel proton-based multifunctional materials, such as hydrogen storage devices and integrated electronic devices.[1,56]

4. Experimental Section

LSMO films were grown on [001]-oriented single crystal substrates by PLD with tunable misfit strains from compressive strains to tensile ones. The deposition parameters were optimized with an oxygen pressure range from 5.0×10^{-4} to 15.0 Pa, a laser fluence of 0.5 J cm^{-2}, a repetition rate of 3 Hz, and a deposition temperature of 720.0 °C. The films were cooled to room temperature at a rate of 20 °C min^{-1} in the same deposition oxygen atmosphere. The thickness of the LSMO films was fixed at 20.0 nm. The epitaxial LSMO thin films were then treated by the hydrogen plasma (Figure 1) at low temperatures ($T \leq 300$ °C) in the LFICP system. The hydrogen flux was fixed at 20 sccm. The plasma treatments were optimized with a power of 1800 W, a voltage bias of –80 V, and a treated time of 5–10 min. The hydrogen cations H^+, rather than H^- or electron *e*, can be injected into LSMO films with the negative voltage bias (–80 V). The HLSMO films were annealed in the PLD chamber for 1 h to release the hydrogen with an oxygen pressure of 100 Pa at 300 °C.

The crystal structure analysis of the LSMO films was characterized by a high-resolution four-circle X-ray diffractometer (XRD, Rigaku-Smartlab, 9 KW). The out-of-plane lattice parameters of the LSMO films were determined by θ–2θ scan, whereas the in-plane lattice parameters and the epitaxy of the films were confirmed by RSM. The thicknesses of the LSMO films were determined by X-ray reflectivity. The magnetic properties of the LSMO films were measured using a PPMS (Quantum Design, EverCool- II). Element-specific X-ray absorption spectra were collected at beamline 4.0.2 of the Advanced Light Source at the Lawrence Berkeley National Laboratory with a grazing incidence angle of 30°.

To directly check the information of hydrogen, SIMS measurements were carried out. During the measurement, a cesium-ion beam (1 KeV) was employed to detect over a region of about 100×100 μm^2. The signals of H, Mn, and Ti were recorded simultaneously. The interface position can be determined by the measured distributions of H, Ti, and Mn (i.e., the gradient distribution region).

The electronic bandgap of the HLSMO film was obtained via the Vienna ab initio simulation package.[57] The core–valence interactions were treated by the projector augmented wave method, where the plane wave expansion is truncated with a cutoff energy of 500 eV. The exchange-correlation functional with the Perdew–Burke–Ernzerhof (PBE) approximation employed. To better determine the ground state, a *k*-mesh with a $2 \times 2 \times 1$ Monkhorst–Pack grid in momentum space is used in self-consistent calculations. The on-site Coulomb repulsion is introduced beyond the generalized gradient approximation (GGA), i.e., GGA+U calculations to fit the strongly correlated effects of 3d electrons in Mn.[58] The value of on-site Coulomb repulsion energy is chosen to be 4 eV. In order to optimize crystalline structures of hydrogenated BM phase for manganite films, a similar composition of $H_{0.5}La_{0.8}Sr_{0.2}MnO_{2.5}$ film was studied as a model system. Various structural possibilities of alternate supercells of HBM manganites, consisting of planar, tetrahedral, pyramidal, or octahedral geometries, were explored.

Supporting Information

Supporting Information is available from the Wiley Online Library or from the author.

Acknowledgements

S.Q.C. and H.P.Z. contributed equally to this work. C.W.H. gratefully acknowledges supports from the Natural Science Foundation of Shenzhen University (SZU) (Grant No. 827-000198). H.P.Z. thanks the supports from Open Project of Key Laboratory Artificial 6 16 Structures and Quantum Control (Ministry of Education) and Fundamental Research Funds for Central Universities (Grant No. ZYGX2016J143). Z.H.C. acknowledges the financial support from the National Natural Science Foundation of China (Grant No. 51802057). L.C. thanks the Science and Technology Research Items of Shenzhen (JCYJ20170412153325679 and JCYJ20180504165650580). S.D. acknowledges the support of the Gordon and Betty Moore Foundation's EPiQS Initiative, under grant GBMF5307. L.Z. acknowledges the support of the Army Research Office under grant W911NF-14-1-0104. E.L. acknowledges the support of the National Science Foundation under grant DMR-1608938. L.W.M. acknowledges the support of the National Science Foundation under grant DMR-1708615. This research used resources of the Advanced Light Source, which is a Department of Energy (DOE) Office of Science User Facility under Contract No. DE-AC02-05CH11231. The affiliation of the authors Haiping Zhou and Xing Ye was revised on December 10, 2019 after initial publication online.

[1] C. G. Van de Walle, J. Neugebauer, *Annu. Rev. Mater. Res.* **2006**, *36*, 179.

[2] H. Kageyama, K. Hayashi, K. Maeda, J. P. Attfield, Z. Hiroi, J. M. Rondinelli, K. R. Poeppelmeier, *Nat. Commun.* **2018**, *9*, 15.

[3] H. Yoon, M. Choi, T. W. Lim, H. Kwon, K. Ihm, J. K. Kim, S. Y. Choi, J. Son, *Nat. Mater.* **2016**, *15*, 1113.

[4] X. Peng, X. Zhang, L. Wang, L. Hu, S. H.-S. Cheng, C. Huang, B. Gao, F. Ma, K. Huo, P. K. Chu, *Adv. Funct. Mater.* **2016**, *26*, 784.

[5] Y. Zhou, X. Guan, H. Zhou, K. Ramadoss, S. Adam, H. Liu, S. Lee, J. Shi, M. Tsuchiya, D. D. Fong, S. Ramanathan, *Nature* **2016**, *534*, 231.

[6] C. Tassel, Y. Goto, Y. Kuno, J. Hester, M. Green, Y. Kobayashi, H. Kageyama, *Angew. Chem., Int. Ed.* **2014**, *53*, 10377.

[7] Y. Cui, G. Zhang, H. Li, H. Lin, X. Zhu, H.-H. Wen, G. Wang, J. Sun, M. Ma, Y. Li, D. Gong, T. Xie, Y. Gu, S. Li, H. Luo, P. Yu, W. Yu, *Sci. Bull.* **2018**, *63*, 11.

[8] N. Lu, P. Zhang, Q. Zhang, R. Qiao, Q. He, H.-B. Li, Y. Wang, J. Guo, D. Zhang, Z. Duan, Z. Li, M. Wang, S. Yang, M. Yan, E. Arenholz, S. Zhou, W. Yang, L. Gu, C.-W. Nan, J. Wu, Y. Tokura, P. Yu, *Nature* **2017**, *546*, 124.

[9] J. Y. Ni, P. S. Wang, J. L. Lu, H. J. Xiang, *Phys. Rev. Lett.* **2019**, *122*, 117601.

[10] S. Chen, Z. Wang, H. Ren, Y. Chen, W. Yan, C. Wang, B. Li, J. Jiang, C. Zou, *Sci. Adv.* **2019**, *5*, eaav6815.

[11] A. Urushibara, Y. Moritomo, T. Arima, A. Asamitsu, G. Kido, Y. Tokura, *Phys. Rev. B* **1995**, *51*, 14103.

[12] M. Imada, A. Fujimori, Y. Tokura, *Rev. Mod. Phys.* **1998**, *70*, 1039.

[13] B. Dabrowski, X. Xiong, Z. Bukowski, R. Dybzinski, P. W. Klamut, J. E. Siewenie, O. Chmaissem, J. Shaffer, C. W. Kimball, J. D. Jorgensen, S. Short, *Phys. Rev. B* **1999**, *60*, 7006.

[14] Z. Liao, M. Huijben, Z. Zhong, N. Gauquelin, S. Macke, R. J. Green, S. Van Aert, J. Verbeeck, G. Van Tendeloo, K. Held, G. A. Sawatzky, G. Koster, G. Rijnders, *Nat. Mater.* **2016**, *15*, 425.

[15] J. Chakhalian, J. W. Freeland, A. J. Millis, C. Panagopoulos, J. M. Rondinelli, *Rev. Mod. Phys.* **2014**, *86*, 1189.

[16] J. M. D. Coey, M. Viret, S. von Molnár, *Adv. Phys.* **1999**, *48*, 167.

[17] H. Y. Hwang, Y. Iwasa, M. Kawasaki, B. Keimer, N. Nagaosa, Y. Tokura, *Nat. Mater.* **2012**, *11*, 103.

[18] R. J. Zeches, M. D. Rossell, J. X. Zhang, A. J. Hatt, Q. He, C.-H. Yang, A. Kumar, C. H. Wang, A. Melville, C. Adamo, G. Sheng, Y.-H. Chu, J. F. Ihlefeld, R. Erni, C. Ederer, V. Gopalan, L. Q. Chen, D. G. Schlom, N. A. Spaldin, L. W. Martin, R. Ramesh, *Science* **2009**, *326*, 977.

[19] X. R. Wang, C. J. Li, W. M. Lü, T. R. Paudel, D. P. Leusink, M. Hoek, N. Poccia, A. Vailionis, T. Venkatesan, J. M. D. Coey, E. Y. Tsymbal, Ariando, H. Hilgenkamp, *Science* **2015**, *349*, 716.

[20] J. A. Mundy, C. M. Brooks, M. E. Holtz, J. A. Moyer, H. Das, A. F. Rebola, J. T. Heron, J. D. Clarkson, S. M. Disseler, Z. Liu, A. Farhan, R. Held, R. Hovden, E. Padgett, Q. Mao, H. Paik, R. Misra, L. F. Kourkoutis, E. Arenholz, A. Scholl, J. A. Borchers, W. D. Ratcliff, R. Ramesh, C. J. Fennie, P. Schiffer, D. A. Muller, D. G. Schlom, *Nature* **2016**, *537*, 523.

[21] X. J. Chen, S. Soltan, H. Zhang, H. U. Habermeier, *Phys. Rev. B* **2002**, *65*, 174402.

[22] C. Aruta, G. Ghiringhelli, A. Tebano, N. G. Boggio, N. B. Brookes, P. G. Medaglia, G. Balestrino, *Phys. Rev. B* **2006**, *73*, 235121.

[23] F. Tsui, M. C. Smoak, T. K. Nath, C. B. Eom, *Appl. Phys. Lett.* **2000**, *76*, 2421.

[24] R. Guo, L. E. Cross, S. E. Park, B. Noheda, D. E. Cox, G. Shirane, *Phys. Rev. Lett.* **2000**, *84*, 5423.

[25] J. Dho, N. H. Hur, I. S. Kim, Y. K. Park, *J. Appl. Phys.* **2003**, *94*, 7670.

[26] J. Sakai, N. Ito, S. Imai, *J. Appl. Phys.* **2006**, *99*, 08Q318.

[27] H. Guo, J.-o. Wang, X. He, Z. Yang, Q. Zhang, K.-j. Jin, C. Ge, R. Zhao, L. Gu, Y. Feng, W. Zhou, X. Li, Q. Wan, M. He, C. Hong, Z. Guo, C. Wang, H. Lu, K. Ibrahim, S. Meng, H. Yang, G. Yang, *Adv. Mater. Interfaces* **2016**, *3*, 1500753.

[28] H. Jeen, W. S. Choi, M. D. Biegalski, C. M. Folkman, I. C. Tung, D. D. Fong, J. W. Freeland, D. Shin, H. Ohta, M. F. Chisholm, H. N. Lee, *Nat. Mater.* **2013**, *12*, 1057.

[29] L. Yao, S. Inkinen, S. van Dijken, *Nat. Commun.* **2017**, *8*, 14544.

[30] S. Chen, C. Guan, S. Ke, X. Zeng, C. Huang, S. Hu, F. Yen, H. Huang, Y. Lu, L. Chen, *ACS Appl. Mater. Interfaces* **2018**, *10*, 18029.

[31] P. Perna, C. Rodrigo, E. Jiménez, F. J. Teran, N. Mikuszeit, L. Méchin, J. Camarero, R. Miranda, *J. Appl. Phys.* **2011**, *110*, 013919.

[32] S. Majumdar, K. Kooser, T. Elovaara, H. Huhtinen, S. Granroth, P. Paturi, *J. Phys.: Condens. Matter* **2013**, *25*, 376003.

[33] H. Boschker, J. Kautz, E. P. Houwman, W. Siemons, D. H. A. Blank, M. Huijben, G. Koster, A. Vailionis, G. Rijnders, *Phys. Rev. Lett.* **2012**, *109*, 157207.

[34] M. Huijben, L. W. Martin, Y. H. Chu, M. B. Holcomb, P. Yu, G. Rijnders, D. H. A. Blank, R. Ramesh, *Phys. Rev. B* **2008**, *78*, 094413.

[35] D. D. Fong, G. B. Stephenson, S. K. Streiffer, J. A. Eastman, O. Auciello, P. H. Fuoss, C. Thompson, *Science* **2004**, *304*, 1650.

[36] E. J. Moon, P. V. Balachandran, B. J. Kirby, D. J. Keavney, R. J. Sichel-Tissot, C. M. Schleputz, E. Karapetrova, X. M. Cheng, J. M. Rondinelli, S. J. May, *Nano Lett.* **2014**, *14*, 2509.

[37] M. Abbate, F. M. F. de Groot, J. C. Fuggle, A. Fujimori, O. Strebel, F. lopez, M. Domke, G. Kaindl, G. A. Sawatzky, M. Takano, Y. Takeda, H. Eisaki, S. Uchida, *Phys. Rev. B* **1992**, *46*, 4511.

[38] Y. Tokura, *Rep. Prog. Phys.* **2006**, *69*, 797.

[39] T. Yajima, A. Kitada, Y. Kobayashi, T. Sakaguchi, G. Bouilly, S. Kasahara, T. Terashima, M. Takano, H. Kageyama, *J. Am. Chem. Soc.* **2012**, *134*, 8782.

[40] M. Pichler, W. Si, F. Haydous, H. Téllez, J. Druce, E. Fabbri, M. E. Kazzi, M. Döbeli, S. Ninova, U. Aschauer, A. Wokaun, D. Pergolesi, T. Lippert, *Adv. Funct. Mater.* **2017**, *27*, 1605690.

[41] Y. Chen, Z. Wang, S. Chen, H. Ren, L. Wang, G. Zhang, Y. Lu, J. Jiang, C. Zou, Y. Luo, *Nat. Commun.* **2018**, *9*, 818.

[42] Y. Kobayashi, O. J. Hernandez, T. Sakaguchi, T. Yajima, T. Roisnel, Y. Tsujimoto, M. Morita, Y. Noda, Y. Mogami, A. Kitada, M. Ohkura, S. Hosokawa, Z. Li, K. Hayashi, Y. Kusano, J. Kim, N. Tsuji, A. Fujiwara, Y. Matsushita, K. Yoshimura, K. Takegoshi, M. Inoue, M. Takano, H. Kageyama, *Nat. Mater.* **2012**, *11*, 507.

[43] T. Yamamoto, D. Zeng, T. Kawakami, V. Arcisauskaite, K. Yata, M. A. Patino, N. Izumo, J. E. McGrady, H. Kageyama, M. A. Hayward, *Nat. Commun.* **2017**, *8*, 1217.

[44] M. A. Hayward, E. J. Cussen, J. B. Claridge, M. Bieringer, M. J. Rosseinsky, C. J. Kiely, S. J. Blundell, I. M. Marshall, F. L. Pratt, *Science* **2002**, *295*, 1882.

[45] M. D'Angelo, R. Yukawa, K. Ozawa, S. Yamamoto, T. Hirahara, S. Hasegawa, M. G. Silly, F. Sirotti, I. Matsuda, *Phys. Rev. Lett.* **2012**, *108*, 116802.

[46] J.-S. Lee, Y. Li, Y. Lin, S. Y. Lee, Q. X. Jia, *Appl. Phys. Lett.* **2004**, *84*, 3825.

[47] K. Xiong, J. Robertson, *Appl. Phys. Lett.* **2004**, *85*, 2577.
[48] L. Cao, O. Petracic, P. Zakalek, A. Weber, U. Rucker, J. Schubert, A. Koutsioubas, S. Mattauch, T. Bruckel, *Adv. Mater.* **2019**, *31*, 1806183.
[49] H. P. Zhou, X. Ye, W. Huang, M. Q. Wu, L. N. Mao, B. Yu, S. Xu, I. Levchenko, K. Bazaka, *ACS Appl. Mater. Interfaces* **2019**, *11*, 15122.
[50] J. D. Ferguson, Y. Kim, L. F. Kourkoutis, A. Vodnick, A. R. Woll, D. A. Muller, J. D. Brock, *Adv. Mater.* **2011**, *23*, 1226.
[51] C. Adamo, X. Ke, H. Q. Wang, H. L. Xin, T. Heeg, M. E. Hawley, W. Zander, J. Schubert, P. Schiffer, D. A. Muller, L. Maritato, D. G. Schlom, *Appl. Phys. Lett.* **2009**, *95*, 112504.
[52] L. Yao, S. Majumdar, L. Akaslompolo, S. Inkinen, Q. H. Qin, S. van Dijken, *Adv. Mater.* **2014**, *26*, 2789.
[53] Z. Chen, Z. Chen, Z. Q. Liu, M. E. Holtz, C. J. Li, X. R. Wang, W. M. Lu, M. Motapothula, L. S. Fan, J. A. Turcaud, L. R. Dedon, C. Frederick, R. J. Xu, R. Gao, A. T. N'Diaye, E. Arenholz, J. A. Mundy, T. Venkatesan, D. A. Muller, L. W. Wang, J. Liu, L. W. Martin, *Phys. Rev. Lett.* **2017**, *119*, 156801.
[54] R. Qiao, T. Chin, S. J. Harris, S. Yan, W. Yang, *Curr. Appl. Phys.* **2013**, *13*, 544.
[55] T. Yamamoto, Y. Kobayashi, N. Hayashi, C. Tassel, T. Saito, S. Yamanaka, M. Takano, K. Ohoyama, Y. Shimakawa, K. Yoshimura, H. Kageyama, *J. Am. Chem. Soc.* **2012**, *134*, 11444.
[56] S.-i. Orimo, Y. Nakamori, J. R. Eliseo, A. Züttel, C. M. Jensen, *Chem. Rev.* **2007**, *107*, 4111.
[57] G. Kresse, J. Furthmüller, *Phys. Rev. B* **1996**, *54*, 11169.
[58] A. I. Liechtenstein, V. I. Anisimov, J. Zaanen, *Phys. Rev. B* **1995**, *52*, R5467.